Composite CrN/HVOF coatings for superior high-temperature wear resistance

Composites Part B 322 (2026) 113748

Contents lists available at ScienceDirect

Composites Part B

journal homepage: www.elsevier.com/locate/compositesb

Composite CrN/HVOF coatings for superior high-temperature wear resistance

Lei Shao [a,*], Ru Liu [a], Wensheng Li [b,**], Yanru Sun [a], Xuedan Song [a], Xiaojie Song [a], Canming Wang [a], Qiang Song [a], Lunlin Shang [c], Sheng Guo [d]

[a] School of Materials Science and Engineering, Shandong University of Science and Technology, Qingdao, 266590, China
[b] School of Metallurgical Engineering, Lanzhou Resources & Environment Voc-Tech University, Lanzhou, 730021, China
[c] State Key Laboratory of Solid Lubrication, Lanzhou Institute of Chemical Physics, Chinese Academy of Sciences, Lanzhou, 730000, China
[d] Industrial and Materials Science, Chalmers University of Technology, Gothenburg, SE-41296, Sweden

ARTICLE INFO

Keywords:
CrN coatings
Composite coating architecture
HVOF interlayer
High-temperature wear
Tribological mechanisms

ABSTRACT

CrN coatings possess excellent hardness but suffer from rapid degradation under high-temperature sliding, largely due to limited toughness and substrate softening. In this work, we introduce a composite coating architecture, consisting of a CrN top layer supported by NiCrBSi or Stellite12 high-velocity oxy-fuel (HVOF) interlayers, designed to improve high-temperature load-bearing capacity and wear performance. Reciprocating sliding tests up to 600 °C demonstrate that the composite systems exhibit substantially reduced wear rates compared with monolithic CrN, enabled primarily by the mechanical support of the HVOF interlayers, which effectively suppress substrate plasticity and crack formation. Cross-sectional TEM of worn regions reveals that CrN accommodates high-temperature deformation through a sequence of dislocation activities, partial dislocation slip generating stacking faults and nanotwins, and stress-assisted amorphization at grain boundaries. While these mechanisms provide additional strain accommodation, they are not sufficient to prevent severe damage in monolithic CrN. In contrast, the composite coating maintains structural integrity and shows a transition to predominantly mild oxidative wear, highlighting the critical role of the interlayer in stabilizing the CrN film under thermomechanical loading. This study demonstrates that engineering a load-bearing composite architecture provides an effective pathway to achieve high-temperature wear resistance in nitride ceramic coatings, while offering new insight into the high-temperature deformation behaviors of CrN.

1. Introduction

With increasing demand for aerospace components operating under severe thermal and mechanical loads, protective coatings must deliver reliable wear resistance at elevated temperatures. Transition metal nitride (TMN) coatings deposited by physical vapor deposition (PVD) have long been used for this purpose owing to their high hardness, oxidation resistance, and thermal stability [1,2]. Binary TMNs such as CrN [3,4], TiN [5,6], ZrN [7], and HfN [8] form the basis of many industrial coating systems, but they increasingly fall short under the complex thermomechanical conditions associated with high-temperature sliding and heavy contact stresses [9]. To address these limitations, research has expanded toward multi-component TMNs [10,11], amorphous–nanocrystalline composites [12], and multilayer or nano-multilayer architectures [13,14], all designed to enhance hardness, thermal stability, and fracture resistance.

Alloying and architectural design offer well-established strengthening routes. For example, the incorporation of Al into CrN or TiN increases hardness through strong Al–N covalent bonding [15], although performance can deteriorate once metastable fcc-AlN decomposes to the stable hexagonal phase [16]. Determining the maximum Al content that preserves the cubic structure remains an active area of research [15,17–20]. CrAlN coatings demonstrate excellent oxidation and wear resistance at elevated temperatures due to the formation of protective Al_2O_3 and lubricious Cr_2O_3 scales [21–23]. Similarly, Si additions promote the formation of amorphous-SiN_x/nanocrystalline-TiN composites, with hardness values exceeding 40 GPa and improved thermal stability [11,24,25]. Multilayer architectures further enhance mechanical

* Corresponding author.
** Corresponding author.
E-mail addresses: shaoleiustb@163.com (L. Shao), liws@lzre.edu.cn (W. Li).

https://doi.org/10.1016/j.compositesb.2026.113748
Received 6 January 2026; Received in revised form 30 April 2026; Accepted 2 May 2026
Available online 4 May 2026

robustness by introducing interfaces that impede dislocation motion, suppress crack propagation, and stabilize metastable phases [26–28].

While these strategies improve the intrinsic mechanical properties of TMN coatings, a critical challenge persists: premature failure driven by substrate softening at elevated temperatures, particularly for lightweight alloys widely used in aerospace applications. Once the substrate plastically deforms, the thin PVD coating can no longer sustain applied stresses, leading to cracking, delamination, and catastrophic wear. Improving the temperature-dependent load-bearing capability of the entire coating–substrate system therefore remains a fundamental and largely unmet requirement.

In response, a hybrid architecture combining PVD films with high-velocity oxy-fuel (HVOF) thermal-sprayed interlayers has attracted growing interest. In these systems, a thick HVOF layer (hundreds of micrometers) provides mechanical support and thermal stability, while a thin PVD top film supplies low friction, high hardness, and surface smoothness. Such a composite design offers several advantages: (i) a mechanically robust interlayer that mitigates substrate plasticity under high-temperature loads; (ii) a gradual transition in hardness and modulus from the ceramic film to the metallic substrate, reducing interfacial stresses; and (iii) improved surface finish and lower friction compared with stand-alone HVOF coatings. Importantly, this architecture also delivers significant wear resistance without increasing weight, a key criterion for aerospace applications. Indeed, our previous work [29] revealed that integrating CrN with NiCrBSi or Stellite12 HVOF interlayers leads to a substantial enhancement in room-temperature wear resistance, highlighting the strong potential of this composite coating concept.

Despite the growing interest in PVD/HVOF composite systems, the high-temperature tribological behavior of such architectures, and the way in which the interlayer modifies deformation mechanisms in the ceramic top film, remains poorly understood. In particular, it is unclear how mechanical support from HVOF coatings influences dislocation activity, grain-boundary processes, and the transition between oxidative, abrasive, and fatigue wear at elevated temperatures. The present work addresses these knowledge gaps by establishing a CrN/HVOF duplex architecture as a model platform to decouple mechanical support effects from intrinsic ceramic deformation behavior. Through controlled high-temperature sliding tests up to 600 °C and correlative TEM analysis of subsurface microstructures, we demonstrate how the load-bearing interlayer fundamentally alters stress distribution, suppresses subsurface cracking, and enables a shift toward mild oxidative wear. This study therefore provides both a mechanistic understanding of high-temperature deformation in CrN and a validated design strategy for achieving robust high-temperature wear resistance through architecture-driven load-bearing support.

2. Experiment

2.1. PVD/HVOF coatings preparation

The NiCrBSi and Stellite12 coatings, produced from powders with a size range of 15-45 μm (supplied by Zhuzhou Sanli Carbide Material Co., Ltd., China), were deposited onto 316L substrates measuring 200 × 100 × 10 mm^3 via HVOF spraying using a JP8000 system (Praxair, USA). The coated substrates were subsequently sectioned into 10 × 10 × 10 mm^3 specimens by wire electrical discharge machining. These specimens were then ground and polished to achieve a surface roughness of Ra ≤1 μm, followed by cleaning with petroleum ether and ethanol. A CrN film was deposited onto the prepared HVOF-coated or bare 316L surfaces using arc ion plating (AIP; Flexicoat 350, Hauzer, Netherlands). Prior to CrN deposition, a pure Cr interlayer was applied to both the HVOF coatings and the 316L substrate to improve film adhesion. The detailed parameters for the HVOF spraying and AIP processes are provided in Ref. [29].

2.2. Microstructure characterization

The crystalline structure of the coatings was characterized by grazing-incidence X-ray diffraction (GIXRD; SmartLab 9 kW, Rigaku, Japan) using Cu Kα radiation. The measurements were performed at a fixed incident angle of 0.5°, with a 2θ scan range from 30° to 90°, a step size of 0.02°, and a counting time of 0.2 s per step. The surface and wear track morphologies were examined using a scanning electron microscope (SEM; Nava Nano450, USA) equipped with an energy-dispersive X-ray spectrometer (EDS; Oxford, X-Max 80, UK). The cross-sectional microstructure of the wear tracks on the CrN and CrN/NiCrBSi samples after friction tests was analyzed by transmission electron microscopy (TEM; Tecnai F30, Netherlands). TEM specimens were prepared using a dual-beam focused ion beam (FIB; Zeiss Auriga, Germany) system via standard lift-out procedures.

2.3. Hardness and tribological testing

High-temperature hardness measurements were conducted using a high temperature module integrated with a tribometer (UMT TriboLab, Bruker, USA). Tests were performed in ambient air at room temperature, 200 °C, 400 °C, and 600 °C. A Rockwell C-scale indentation method was applied, employing a Φ6 mm Si_3N_4 ball indenter under a preload of 98 N and a total load of 1471 N. The sample was heated to each target temperature at a rate of 15 °C/min and held for 5 min prior to testing to ensure thermal stability. Four indentations were made under each condition to ensure statistical reliability. Wear tests were performed on the same UMT TriboLab tribometer using a pin-on-disc configuration with an Al_2O_3 ball (Φ6 mm) as the counterface. Tests were carried out at 200 °C, 400 °C, and 600 °C in air under a normal load of 10 N, a sliding frequency of 1 Hz, a stroke length of 5 mm, and a test duration of 180 s. The wear volume was quantified using a three-dimensional optical profiler (Contour GT-K1, Bruker, USA). Among these, the ASTM G99-23 standard is used to evaluate wear.

3. Results

3.1. Phase structure and high-temperature hardness

Fig. 1 presents the GIXRD patterns of CrN, CrN/NiCrBSi, and CrN/Stellite12 coatings at RT, 200 °C, 400 °C and 600 °C. All three coatings exhibit a face-centered cubic (fcc) phase structure. With increasing temperature, the diffraction peak intensities increase while the full-width-at-half-maximum (FWHM) values decrease. This total peak broadening (β_T) is primarily governed by crystallite size (β_D) and microstrain (β_ε) contributions, as described by the Williamson-Hall equation [30]:

$$\beta_T = \beta_D + \beta_\varepsilon \tag{1}$$

$$\beta_D = \frac{K\lambda}{\mathrm{D}\cos\theta} \tag{2}$$

$$\beta_\varepsilon = 4\varepsilon \tan\theta \tag{3}$$

$$\beta_\mathrm{T} = \frac{K\lambda}{D\cos\theta} + 4\varepsilon\tan\theta \tag{4}$$

where K is Scherrer constant, λ is wavelength of X-ray, D is average crystalline size, θ is diffraction angle, ε is the average lattice strain. Calculated crystallite sizes for the CrN phase are 9.16 nm (200 °C), 12.56 nm (400 °C), and 14.43 nm (600 °C), confirming progressive grain growth with rising temperature. At room temperature, the CrN diffraction peaks are shifted to lower angles relative to the standard PDF reference, indicating lattice expansion of CrN. This phenomenon may be caused by residual stress, solid solution formation, or internal lattice defects. Residual stress in PVD CrN films mainly consist of thermal

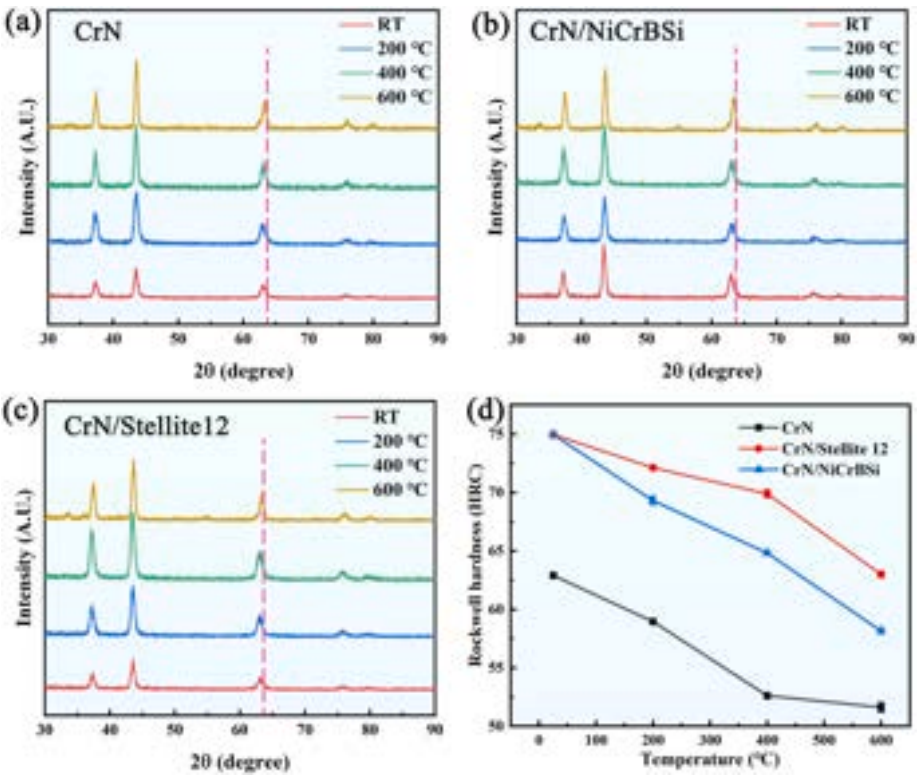

Fig. 1. GIXRD of (a) CrN, (b) CrN/NiCrBSi and (c) CrN/Stellite12 at RT, 200 °C, 400 °C and 600 °C, and the corresponding high-temperature hardness (d).

stress, extrinsic stress and intrinsic stress [31]. Thermal and extrinsic stresses originate primarily from differences in coefficients of thermal expansion (CTE) between the film and substrate and lattice mismatch. Intrinsic stress mainly consists of tensile stress caused by the volume contraction during grain growth, compressive stress caused by the diffusion of adsorbed atoms to the grain boundaries and particle

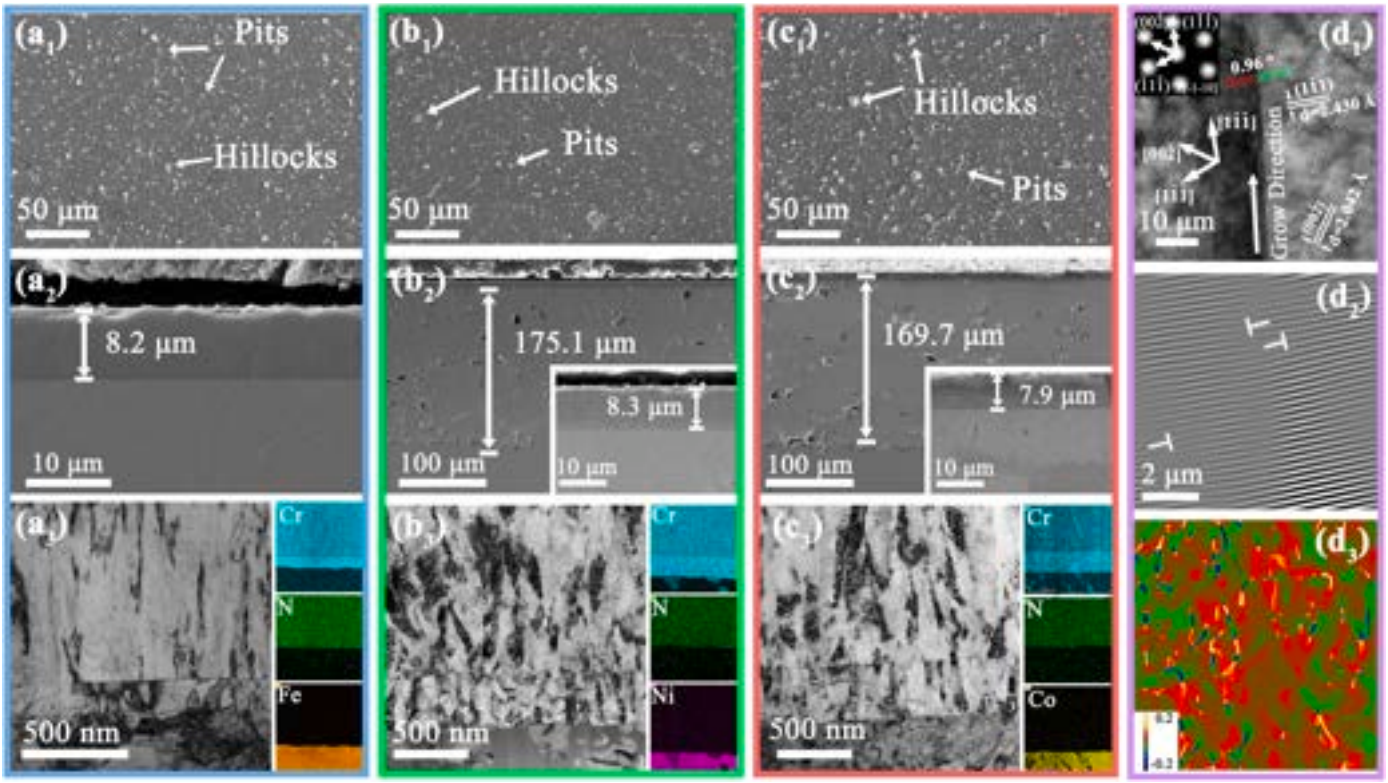

Fig. 2. Surface (a_1, b_1, c_1), cross-sectional (a_2, b_2, c_2) morphology, the TEM image (a_3, b_3, c_3) of CrN, CrN/NiCrBSi and CrN/Stellite12 coatings, HRTEM, the corresponding IFFT and GPA of CrN.

bombardment during deposition [32]. Elevated temperatures enhance atomic diffusion, leading to gradual relaxation of microstrain in the CrN film. Consequently, the diffraction peaks progressively shift toward the standard reference positions. The high-temperatre hardness tests are conducted as shown in Fig. 1(d). It should be noted that measured hardness is not the intrinsic hardness of the thin CrN top layer alone, but rather the composite hardness of the entire coating-substrate system (CrN/HVOF/316L) or CrN/316L system. The composite coating (CrN/HVOF/316L) demonstrates higher hardness than the CrN/316L at both room and elevated temperatures. The hardness of CrN/316L decreases rapidly with increasing temperature, in contrast to the composite coating, which maintains higher hardness due to the reinforcing effect of its Ni-based and Co-based interlayers.

3.2. Microstructure

Fig. 2 presents surface and cross-sectional morphology of the coatings. The CrN surface exhibits characteristic arc-ion-plated features, including hillocks and pits (Fig. 2a_1, b_1, c_1). These features originate from molten target droplets deposited during arcing, where subsequent particle bombardment dislodges some hillocks, leaving corresponding pits. Cross-sectional analysis (Fig. 2a_2, b_2, c_2) reveals a ~8 μm thick CrN layer atop a ~170 μm HVOF coating. Interfaces between CrN/HVOF and HVOF/substrate appear distinct and planar, with no observable delamination or defects. The HVOF coating exhibits limited porosity (~1.5%, ASTM E2109-01), consistent with optimized thermal spray processing. The coating and substrate are mechanically bonded. TEM analysis (Fig. 2(c)) identifies a ~200 nm Cr interlayer between CrN and HVOF/substrate. The Cr interlayer exhibits a dense, continuous structure without observable cracks or voids at the interfaces, which is expected to contribute to enhanced adhesion. The CrN microstructure evolves from fine equiaxed grains (~20-50 nm) at the interface to columnar crystals with increasing diameter (Fig. 2(c)). This transition reflects competitive growth during deposition, where favorably oriented grains dominate the growth front. High-resolution TEM (Fig. 2(d)) reveals adjacent CrN grains sharing a common [111] growth direction. These grains form a low-angle grain boundary (LAGB, 0.96°) comprising an edge dislocation array. Intragranular analysis shows lattice distortions and growth-related dislocations, while geometric phase analysis (GPA) quantifies residual microstrain between grains about 0.2%.

3.3. Coefficients of friction and wear rates

Fig. 3(a–d) presents the CoF and wear rates of CrN, CrN/NiCrBSi, and CrN/Stellite12 coatings at elevated temperatures. The CoF curves exhibit two characteristic stages for all coatings: an initial running-in period followed by a stable stage. At 200 °C, the running-in stage is prolonged and exhibits significant CoF instability. This behavior stems from interacting surface asperities on both the coating and counterpart ball, which reduce the effective contact area and elevate localized contact stresses. Consequently, friction response becomes highly variable during initial sliding. Compared with the hardness at 400 °C and 600 °C, the material exhibits higher hardness at 200 °C, due to the thermal softening effect, which makes surface protrusions more resistant to abrasion and consequently extends the running-in period.

Progressive asperity removal occurs through combined normal loading and shear-induced plastic deformation. This process increases real contact area and transitions friction to a stable regime characterized by lower CoF magnitude and reduced fluctuation amplitude. Periodic formation and ejection of wear debris during stable sliding generate characteristic sawtooth-like CoF oscillations. Increasing temperature reduces both mean CoF values and oscillation amplitudes. This trend is attributed to thermally activated tribo-oxidation, synergistic frictional heating and ambient temperature accelerate formation of low-shear-strength oxide tribofilms at the sliding interface (Figs. 6–9). These oxides act as solid lubricants, reducing shear resistance and stabilizing frictional response [28,30].

Fig. 3(e) shows the 3D and 2D profile of the three coatings. At 200 °C, CrN exhibits significantly greater wear depth and width than CrN/NiCrBSi and CrN/Stellite12 coatings. Maximum wear dimensions occur at 400 °C, where CrN reaches 5.65 μm depth, notably less than its total thickness (8 μm), confirming no coating penetration. At 600 °C, both the wear depth and width decreased. Distinct material accumulation (debris piles or plastic deformation ridges) flanks CrN wear tracks at all temperatures. In contrast, CrN/HVOF coatings develop such features only at 600 °C. This differential behavior demonstrates superior wear resistance of composite coatings across the temperature range, attributable to their enhanced load-bearing capacity and retained hardness at elevated

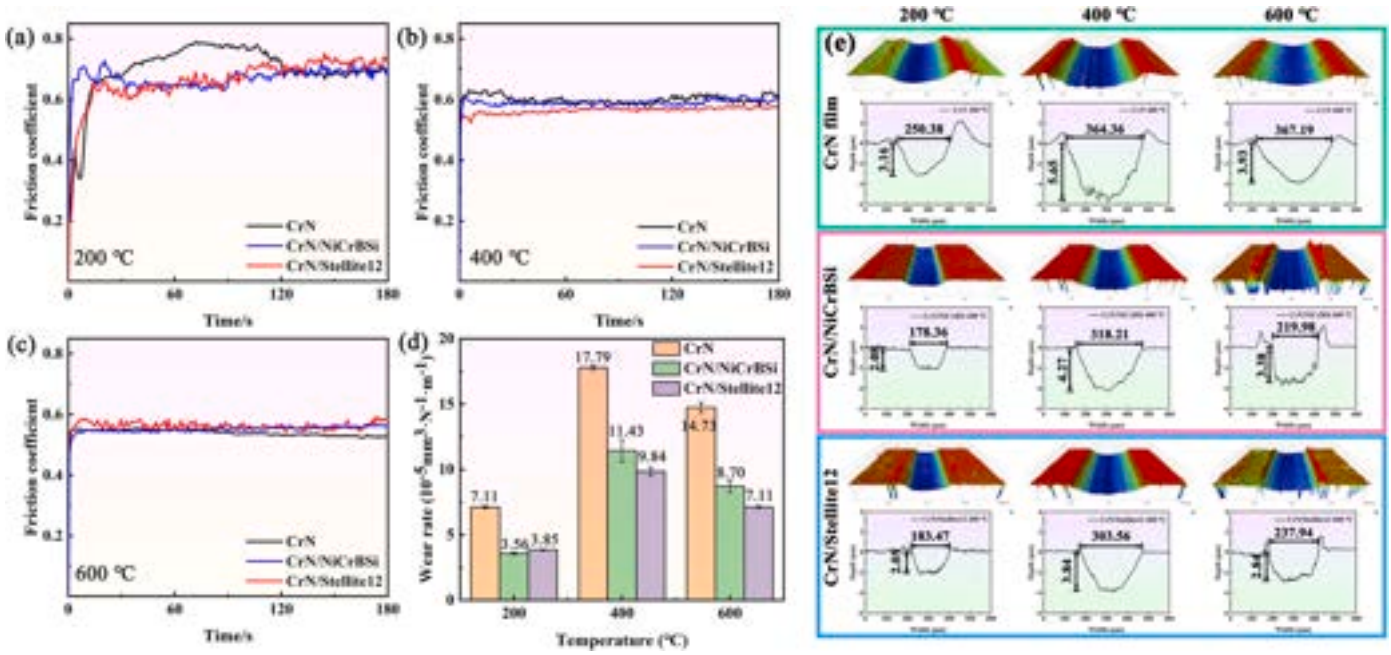

Fig. 3. CoF (a-c), wear rates (d) and the corresponding 3D and 2D profile (e) of CrN, CrN/NiCrBSi and CrN/Stellite12 coatings.

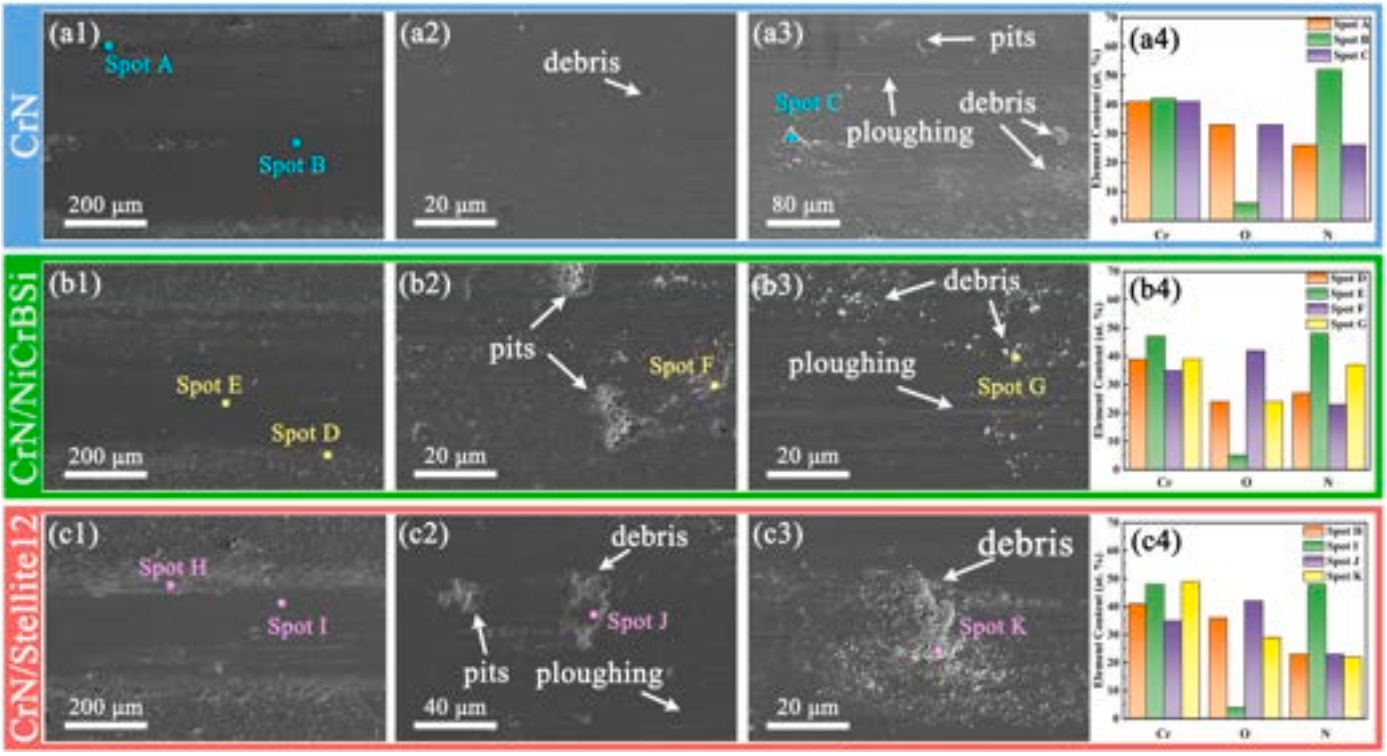

Fig. 4. Wear track and the EDS results of CrN (a_1-a_4), CrN/NiCrBSi (b_1-b_4) and CrN/Stellite12 (c_1-c_4) at 200 °C.

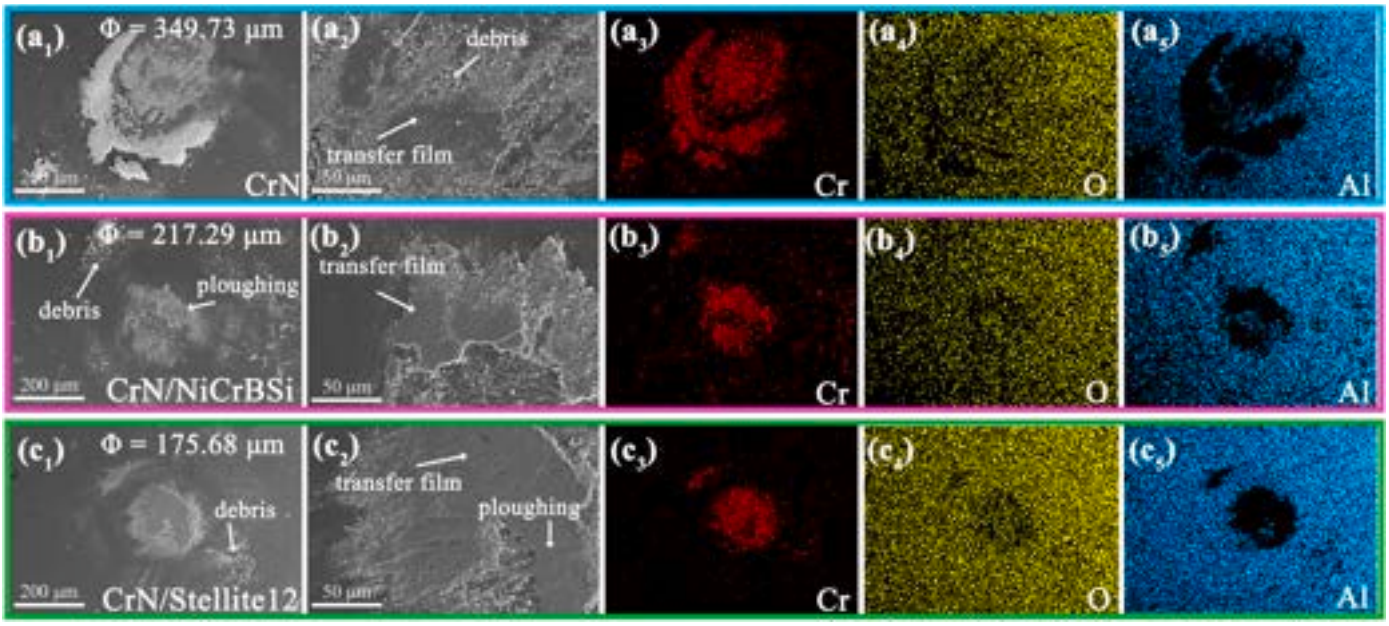

Fig. 5. The wear scars and the EDS mappings on the Al_2O_3 ball corresponding to CrN (a_1-a_5), CrN/NiCrBSi (b_1-b_5) and CrN/Stellite12 (c_1-c_5) at 200 °C.

temperatures. The improved performance further correlates with higher H/E and H^3/E^2 in composite coatings, which effectively inhibit plastic deformation and crack propagation [29]. The wear rates of the three coatings at different temperatures are shown in Fig. 3(d). As the temperature increases, the wear rate shows a trend of first increasing and then decreasing. The wear rate of CrN is always higher than that of CrN/HVOF coatings regardless of the temperature, indicating that even at high temperatures, the CrN/HVOF coatings still have better wear resistance. At 200 °C, the wear rates of the CrN, CrN/NiCrBSi and CrN/Stellite12 coatings are 7.11, 3.56 and 3.85 $mm^3\ N^{-1}\ m^{-1}$ respectively, while at 400 °C, their wear rates increase sharply to 17.79, 11.43 and 9.84 $mm^3\ N^{-1}\ m^{-1}$. According to the Archard equation:

$$W = k\frac{L \cdot S}{H} \tag{5}$$

where W is the wear volume, k is the CoF, L is load, S is the sliding distance, H is hardness. W is inversely proportional to H. Generally speaking, the higher the hardness, the lower the wear rate. Therefore, when the temperature rises to 400 °C, the material hardness decreases, the wear resistance deteriorates, and the wear rate increases. However,

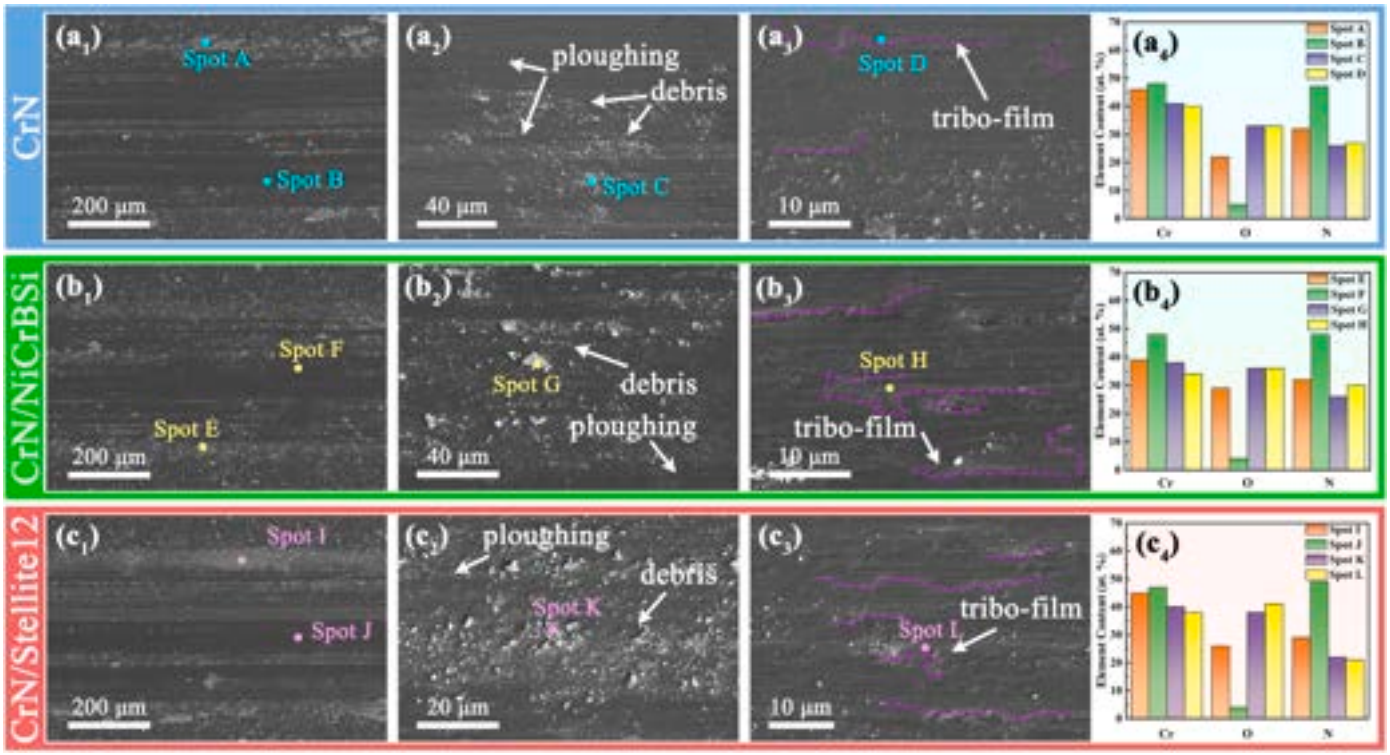

Fig. 6. Wear track and the EDS results of CrN (a_1-a_4), CrN/NiCrBSi (b_1-b_4) and CrN/Stellite12 (c_1-c_4) at 400 °C.

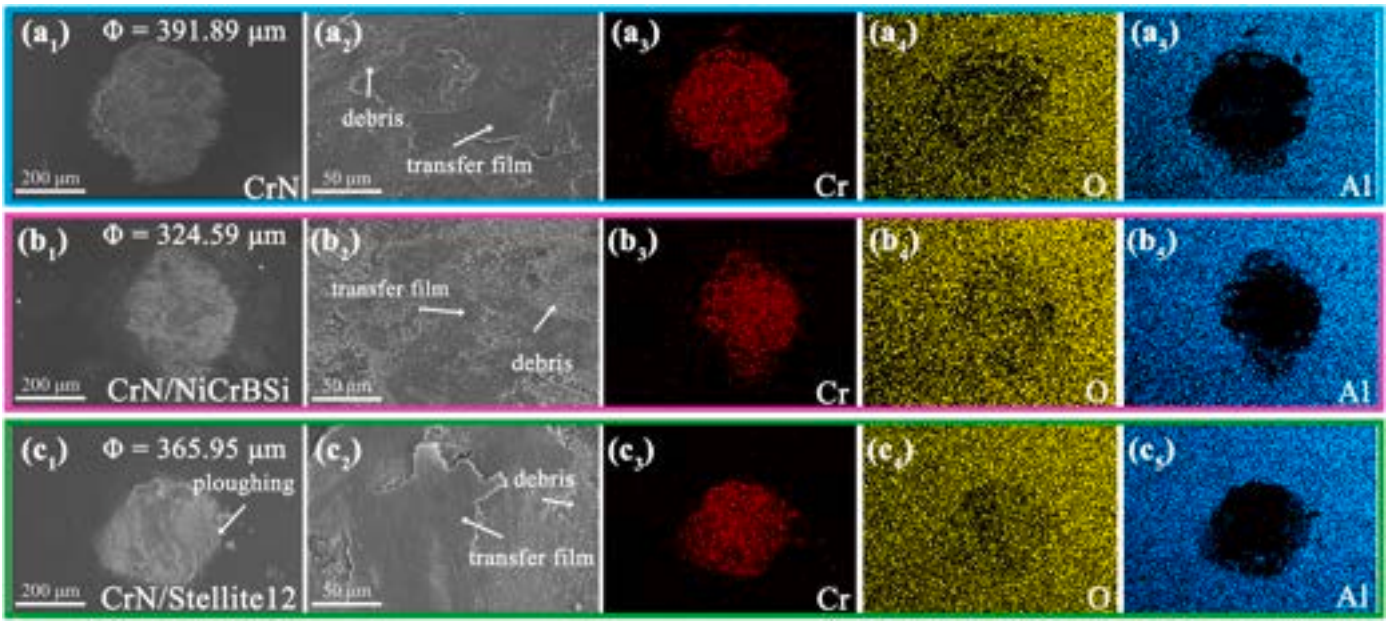

Fig. 7. The wear scars and the EDS mappings on the Al_2O_3 ball corresponding to CrN (a_1-a_5), CrN/NiCrBSi (b_1-b_5) and CrN/Stellite12 (c_1-c_5) at 400 °C.

at 600 °C, the wear rate does not increase with the rise in temperature, instead, it shows a decreasing trend, for example, CrN/Stellite12 has a 27.6% decrease in wear rate. This might be related to the wear mechanism resulting from the coupling effect of friction and temperature. In the following text, the wear mechanism will be analyzed in detail based on the morphology of the wear tracks.

3.4. Characterization of wear tracks and the wear mechanism

3.4.1. Characterization of wear tracks and the wear mechanism at 200 °C

Figs. 4 and 5 show the wear track morphologies on the CrN, CrN/NiCrBSi, and CrN/Stellite12 coatings, along with the corresponding wear scars on Al_2O_3 balls, after sliding tests at 200 °C. The wear track width of the CrN coating is significantly larger than those of the CrN/HVOF coatings. Shallow grooves are observed within all wear tracks, accompanied by debris accumulation at the track edges. This is attributed to the fact that during the friction process, wear debris sheared

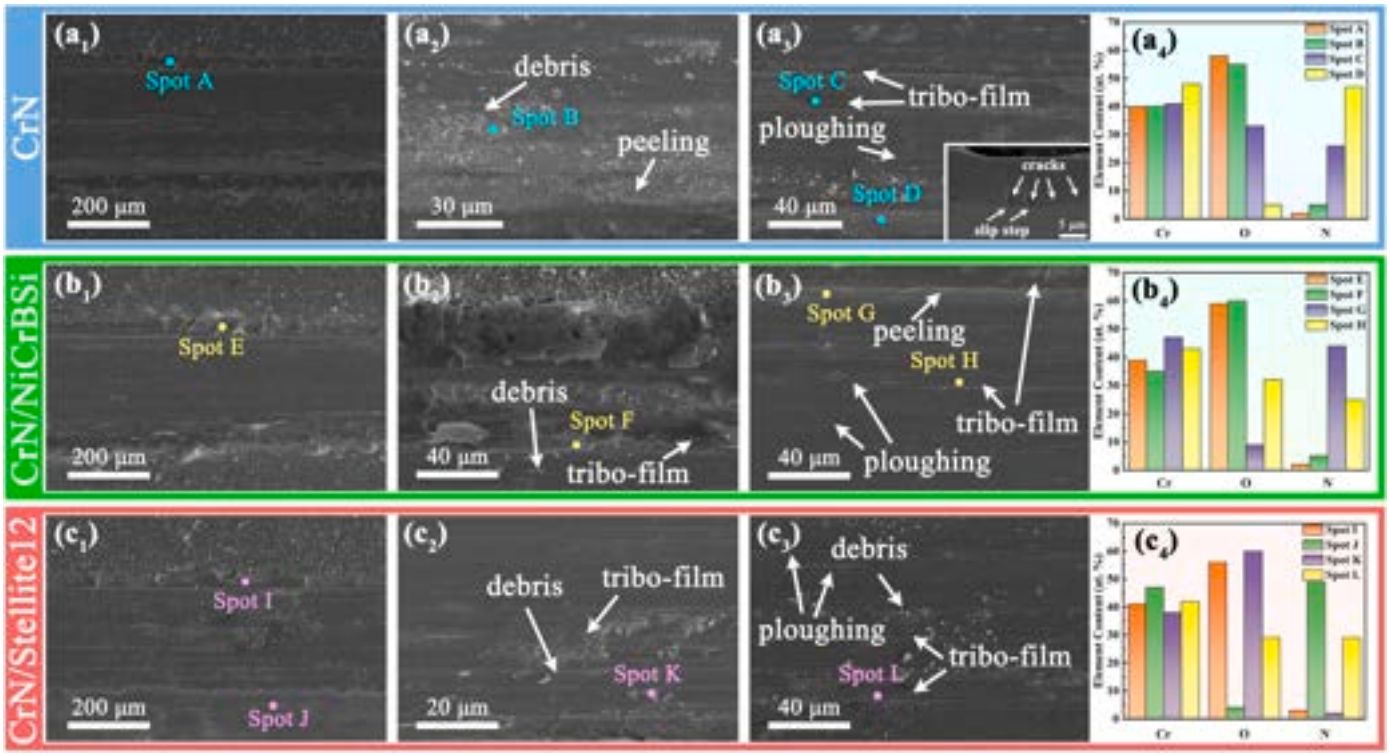

Fig. 8. Wear track and the EDS results of CrN (a_1-a_4), CrN/NiCrBSi (b_1-b_4) and CrN/Stellite12 (c_1-c_4) at 600 °C.

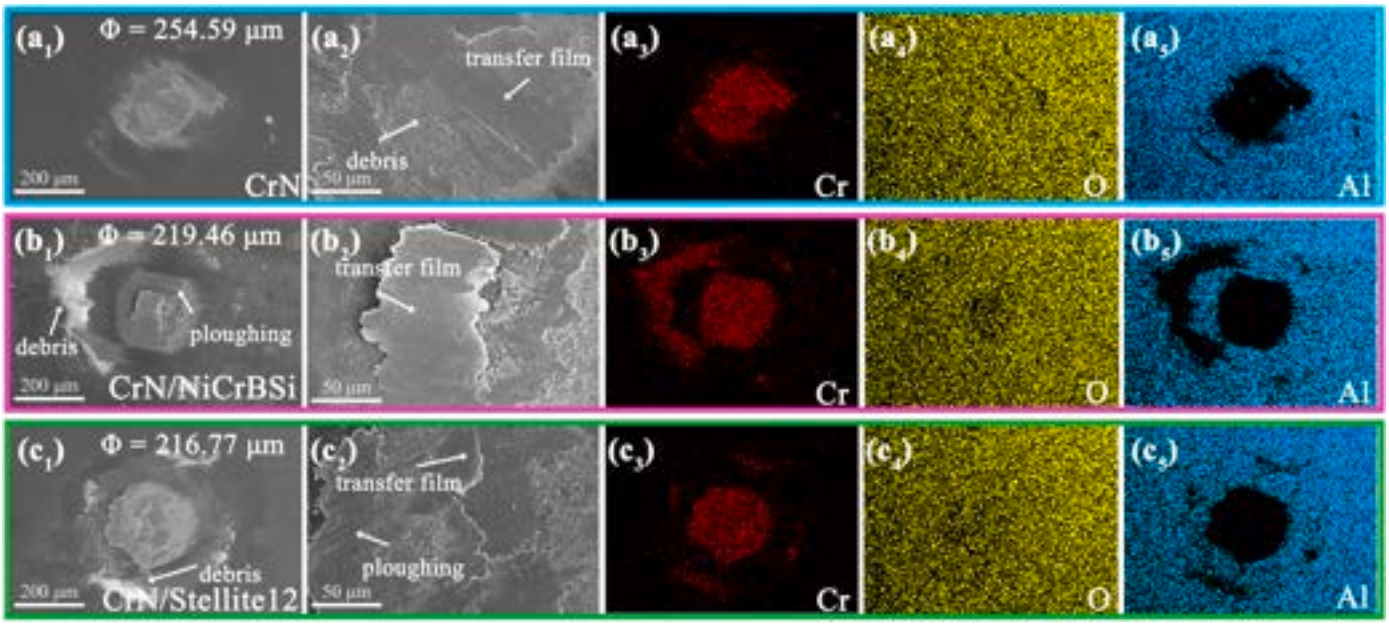

Fig. 9. The wear scars and the EDS mappings on the Al_2O_3 ball corresponding to CrN (a_1-a_5), CrN/NiCrBSi (b_1-b_5) and CrN/Stellite12 (c_1-c_5) at 600 °C.

from the coatings surfaces are not effectively removed from the wear track. These debris subsequently moved with the Al_2O_3 ball, ploughing the coatings surfaces and generating the observed grooves. This debris entrapment and ploughing action are also responsible for the fluctuations of the CoF. These wear debris particles were dispersed across the wear scar surface and underwent slight oxidation due to the combined effect of ambient temperature and frictional heat (Fig. 4a_3-c_3 and a_4-c_4). Under the action of the friction load, those loose debris undergoes compaction, a transfer film with lubricating properties is formed on the Al_2O_3 ball (Fig. 5). The formation of this compacted tribolayer contributes, to some extent, to improve the wear performance. The wear scar of Al_2O_3 ball corresponding to CrN film is the largest, exhibiting the poorest wear resistance, which is consistent with its widest wear track width. Due to its higher hardness and lower wear rate at 200 °C, the composite coating exhibited a shallower wear scar. Consequently, the surface pits remained intact within the worn surface instead of being worn away (Fig. 4b_2 and c_2). The wear scars exhibited negligible oxidation at 200 °C, with very low oxygen content (as indicated by Spot B, E, and I). As a result, the predominant wear mechanism for both the CrN and CrN/HVOF coatings at this temperature was identified as

abrasive wear.

3.4.2. Characterization of wear tracks and the wear mechanism at 400 °C

The wear track morphologies of the CrN and CrN/HVOF coatings at 400 °C are shown in Fig. 6. A significant increase in the number of grooves within the wear tracks is evident, along with a large amount of wear debris dispersed across the surface. This indicates that abrasive wear became more severe for all three coatings at 400 °C. As shown in Fig. 6(a_3, b_3, c_3), localized tribolayers (marked by purple dashed lines) are observed on the wear track surfaces. These layers are formed by the compaction of wear debris. According to EDS analysis, both of debris and the tribolayers exhibited high O content. Under the combined influence of ambient temperature and frictional heating, oxidation initially occurred within the friction contact zone. Due to the relatively slow oxidation kinetics at 400 °C, localized oxide films developed on the friction surface instead of forming a continuous, dense oxide layer. These localized oxide films subsequently spalling under cyclic loading, generating wear debris. A substantial amount of debris participated in the friction process as third-body particles, exacerbating wear. Consequently, the wear rates of all three coatings reached their highest values at 400 °C. In contrast to the wear track morphology, the Al_2O_3 ball does not exhibit a large amount of loose wear debris. Instead, a relatively continuous transfer film is present (Fig. 7). This suggests that friction is severe, generating significant wear debris which was subsequently compacted to form this intact transfer film. According to EDS results, the transfer film consisted predominantly of Cr_2O_3 and also provided the lubricating effect. In summary, at 400 °C, the dominant wear mechanisms for the CrN and CrN/HVOF coatings are abrasive wear accompanied by mild oxidative wear.

3.4.3. Characterization of wear tracks and the wear mechanism at 600 °C

At an 600 °C, extensive tribolayers formed on both sides of the wear tracks for all three coatings. Wear debris generated during friction is expelled to the track peripheries and compacted under stress. As sliding progressed, these compacted tribolayers fractured under shear stress. As shown in Fig. 8(b) and (c), a relatively continuous and intact tribolayer developed within the wear track of the CrN/HVOF coatings. In contrast, the wear track of the CrN contained substantial debris and spalling, indicating that the tribolayer formed on its surface and undergoes spalling during sliding. Examination of the cross-sectional morphology of the CrN wear track at 600 °C revealed that the 316L substrate experienced plastic deformation, generating distinct slip steps. Furthermore, numerous cracks propagating along the columnar grain boundaries are observed within the CrN film, signifying the occurrence of fatigue wear. The CrN film exhibits a typical columnar grain structure (Fig. 2). During the growth of columnar grains, atomic arrangements at the boundaries become less ordered, resulting in grain boundary strength lower than that within the grains. Under frictional loading, stress concentration occurs at the grain boundaries, and fatigue cracks preferentially propagate along these boundaries. In comparison, the high hardness of the HVOF coatings prevent plastic deformation of the substrate. This provided enhanced mechanical support for the CrN top layer, thereby avoiding fatigue failure. Consequently, a continuous tribolayer formed on the surface of the CrN/HVOF coatings. Intact transfer films, primarily composed of Cr_2O_3, are also present on the wear scars of the Al_2O_3 counter balls (Fig. 9). The formation of both tribolayers (on the coating) and transfer films (on the ball) prevent direct contact between the friction surfaces and the Al_2O_3 ball. This reduced the interfacial shear stress, consequently lowering the CoF and enhancing wear resistance. In summary, the wear mechanisms for the monolithic CrN film involved oxidative, fatigue, and abrasive wear, while for the CrN/HVOF coatings, oxidative wear is the primary mechanism.

4. Discussion

4.1. The contact stress during the friction

Contact stress magnitude varies significantly with interfacial geometry in tribological systems, Three fundamental contact modes exist: surface contact, line contact and point contact. Surface contact is characterized by large apparent contact area, generating low mean contact pressure (typically<200 MPa). Line contact exhibits intermediate pressure distribution (1-2 GPa) along elongated interfaces. The concentrated stress fields reaching 4-6 GPa of point contact, due to minimal real contact area. CrN coatings leverage their exceptional hardness (≥25 GPa) specifically for high-stress applications, predominantly employing point-contact configurations. According to the Hertz contact theory [33], the contact radius R can be expressed by the following equation:

$$R = \sqrt[3]{\frac{3PR^*}{4E^*}} \tag{6}$$

where P is the load, R* and E* are the equivalent radius and elastic modulus.

$$\frac{1}{R^*} = \frac{1}{R_1} + \frac{1}{R_2} \tag{7}$$

$$\frac{1}{E^*} = \frac{1-\vartheta_1^2}{E_1} + \frac{1-\vartheta_2^2}{E_2} \tag{8}$$

R_1 and R_2 are the radius of Al_2O_3 ball and the sample. The radius of Al_2O_3 is 3 mm, the sample is cube, so, R_2 can be regarded as ∞. E_1, E_2 and υ_1, υ_2 are the elastic modulus and Poisson's ratio of Al_2O_3 ball and the coating. Therefore, the Hertz contact stress P_H is:

$$P_H = \left(\frac{3P}{2\pi R^2}\right) = \left(\frac{6PE^{*2}}{\pi R^{*2}}\right) \tag{9}$$

According to Eq. (9), the contact stresses of CrN, CrN/NiCrBSi and CrN/Stellite12 at 10 N are 1897, 1792 and 1805 MPa respectively. In the stress zone, the contact stress decreases with the increase of the contact distance. The Hertz contact stress at the distance d from the contact center is:

$$P(d) = P\left(1 - \frac{d^2}{R^2}\right)^{1/2} \tag{10}$$

During the friction process, except for the normal stress, there is also horizontal friction which causes the shear effect on the coating. The shear stress can be expressed:

$$\tau(d) = \mu P(d) = \mu P\left(1 - \frac{d^2}{R^2}\right)^{1/2} \tag{11}$$

Fig. 10 is the bright field (BF) TEM cross-section of the CrN wear track after 600 °C sliding. Three distinct microstructural zones evolve from surface to CrN film substrate: equiaxed nanograin layer, plastic deformation layer and undeformed layer (columnar grain). This graded structure results from depth-dependent stress attenuation during friction. The thickness of the equiaxed nanograin layer is about 460 nm, according to Eqs. (10) and (11), the normal and shear stress in the equiaxed nanograin layer is 1.89 and 1.01 GPa. Similarly, the minimum shear stress in the plastic deformation layer is 0.98 GPa. In undeformed layer, the grains remain columnar without plastic deformation, indicating that the stress in this region is less than the yield stress. Zauner [34] found the yield stress of CrN coating is 6.0 ± 0.4 GPa tested by the micro-pillar at room temperature, and showed the brittle fracture. In this study, the CrN coating is tested at 600 °C under cyclic load with the yield stress 0.98 GPa, and shows the obvious plastic deformation.

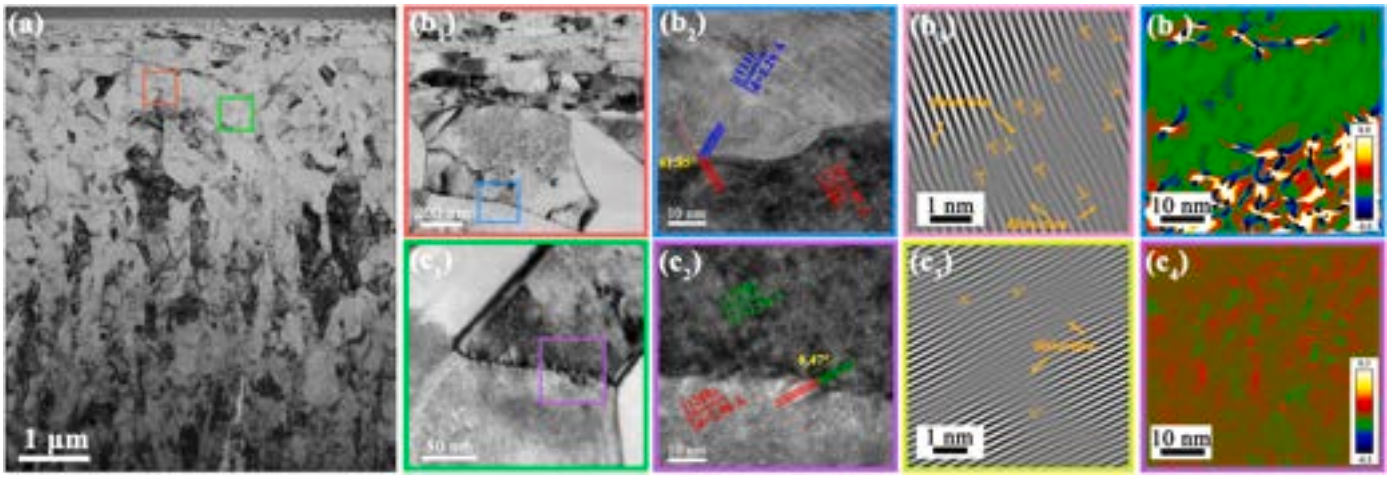

Fig. 10. Cross-sectional TEM of the CrN wear track. (a) Overview, (b_1) GNDs at a bending grain boundary, with (b_2) HRTEM, (b_3) IFFT, and (b_4) GPA. (c_1) Subgrain boundary from dislocation pile-up, with (c_2) HRTEM, (c_3) IFFT, and (c_4) GPA.

4.2. Deformation mechanism

At room temperature, the metal nitride coatings have a high Peierls-Nabarro (P–N) stress due to the covalent bond with high bonding energy. The high P–N stress blocks the movement of dislocation and leading to the low plasticity. Therefore, the sliding of columnar crystals at grain boundaries is the main deformation mechanism of metal nitride deformation at room temperature [35,36]. However, the deformation mechanism of CrN coating at high-temperature, especially under cyclic loads, remains unclear.

In this paper, the deformation mechanism of CrN at high-temperature is revealed by TEM on the wear track. Elevated temperature significantly enhances atomic thermal vibration, activating dislocations within the CrN film. This dislocation activity facilitates plastic deformation of the grains. Fig. 10 is the TEM bright field (BF) image of the wear track of CrN tested at 600 °C. There are three different microstructures, from top to bottom are equiaxed nanograin layer, plastic deformation layer and undeformed layer. This stratification arises from stress gradients generated during frictional contact. As can be seen in Fig. 10(a) and (b_1), the grain boundaries bend under applied load, which is caused by the geometrically necessary dislocations (GNDs) [37,38]. Cyclic loading induces a gradient strain field beneath the wear track, with strain magnitude decaying with distance from the contact center. GNDs nucleate and propagate under this strain gradient to accommodate deformation incompatibility [39,40]. High-resolution TEM (HRTEM) and corresponding inverse fast Fourier transform (IFFT) analyses at curved grain boundaries (Fig. 10(b_2-b_3)) reveal severe lattice distortion and abundant dislocations. The 61.85° misorientation between adjacent grains confirms these are high-angle grain boundaries (HAGBs). Geometric phase analysis (GPA) in Fig. 10(b_4) demonstrates significant strain concentration at the HAGB, consistent with pronounced lattice distortion. Grain boundary bending generates asymmetric strain states between the boundary's compressive and tensile sides, necessitating GND-mediated deformation accommodation to prevent interfacial cracking.

In addition to the GNDs, the grain retains deposited dislocations introduced during the CrN film deposition process. During plastic deformation, these deposited dislocations initiate motion, tangle, and form pile-ups. This dislocation activity leads to the development of subgrain boundaries, effectively fragmenting the initial large columnar grains into smaller equiaxed subgrains. Fig. 10(c_1) presents a subgrain boundary formed by the pile-up of deposited dislocations. The corresponding HRTEM image (c_2) reveals a semi-coherent interface with a misorientation angle of 0.47° between the adjacent subgrains. This low misorientation angle confirms the boundary as a low-angle grain boundary (LAGB). Compared to the HAGBs discussed earlier, the LAGB exhibits significantly reduced dislocation density and lattice distortion, as evidenced in Fig. 10(c_3). Consequently, the microscopic strain localized at the LAGB is substantially lower, as quantified in Fig. 10(c_4). The cooperative activity of GNDs and deposited dislocations governs the plastic deformation response of the CrN.

Secondly, partial dislocation activity is also activated at 600 °C. When the movement of full dislocations is impeded, they dissociate into two partial dislocations to reduce the slip resistance. A critical parameter governing partial dislocation slip is the inherent stacking fault energy (SFE). Generally, lower SFE promotes easier formation of stacking faults (SFs) via shear-induced displacement between adjacent slip planes [41]. Metal nitrides, characterized by strong covalent bonding, exhibit high SFE. For CrN, the SFE is reported as 1110 mJ/m^2 [42], substantially higher than that of Cu (45 mJ/m^2) and Ag (20 mJ/m^2) [43,44]. Consequently, CrN requires significantly higher critical shear stress to nucleate SFs or twins, rendering their formation unfavorable at room temperature. However, this study reveals the presence of SFs and nanotwins within the plastic deformation layer (Fig. 11). The occurrence of SFs or twins in high-SFE ceramics, while challenging, is documented. For instance, c-BN [45,46] and diamond [47] with high-density nanotwins have been synthesized under extreme high-pressure, high-temperature conditions. Similarly, $\sum 3\{112\}$ incoherent twin boundaries (ITBs) have been observed in CrN/AlN superlattice coatings, attributed to interface engineering effects [48]. Furthermore, applied mechanical loading can induce SF or twin formation in metal nitride coatings. Within regions experiencing high strain rates or stresses, the glide of Shockley partial dislocations can lead to twin formation [49]. In the present work, under high-stress reciprocating sliding at 600 °C, partial dislocations in the CrN film undergo slip. This activity facilitates the formation of SFs and twins, serving as an additional accommodation mechanism alongside full dislocation glide. According to the BF image (Fig. 11(a)) and the corresponding selected area electron diffraction (SAED) pattern, the observed SFs lie on (200) crystal plane. This preferential formation is attributed to the relatively lower SFE associated with these planes [50,51]. Chen et al. demonstrated the mechanical significance of SFs by comparing TiN/AlN coatings with and without SFs using micro-pillar compression tests. Their results revealed that SFs impede dislocation glide and crack propagation, thereby enhancing mechanical properties [52]. Similarly, Zhang et al. reported increased hardness in Al/Ti coatings containing a high density of SFs compared to pure Al or Ti coatings [53]. This strengthening effect arises because SFs generate oscillatory stress fields that hinder dislocation motion (Fig. 11 (c)). Nanotwins are also observed within the plastic deformation layer, as shown in Fig. 11(d). Analysis identifies the twinning plane as (220),

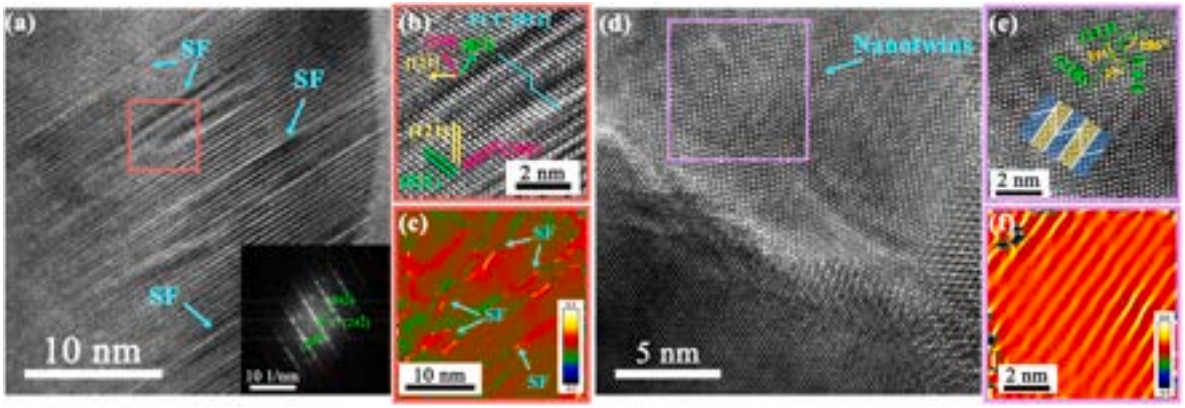

Fig. 11. Stacking fault (a) with the corresponding HRTEM (b) and GPA (c), and nanotwins (d) with the corresponding HRTEM (e) and GPA (f) in plastic deformation layer of CrN film.

the misorientation angle across this twin boundary is approximately 37°. Unlike simple metal lattices, CrN possesses a complex rock-salt structure comprising alternating Cr and N atomic layers. Crucially, the SFE differs significantly between these layers, the SFE for the N atomic plane is markedly lower than for the Cr plane [54]. Consequently, twinning in CrN preferentially occurs on the N-rich atomic planes. Twin boundaries (TBs) act as effective barriers to dislocation motion within the twin, causing dislocations to pile up. As deformation progresses, dislocations attempting to traverse the boundary encounter significantly higher resistance due to the crystallographic misorientation across the coherent TB [55]. This barrier effect enhances strain hardening. The toughening potential of nanotwins is exemplified by Tian's work on diamond, where cracks propagating along (111) planes were deflected into a zigzag path upon encountering TBs, substantially improving fracture toughness [56]. Therefore, the presence of SFs and nano twins improves the deformation ability of CrN coating at high-temperature.

Thirdly, within the nanocrystalline region near the wear track surface, amorphization induced by excessive lattice distortion is observed at grain boundaries (GBs). In this severely deformed zone, grains are refined to 10–50 nm with significantly increased subgrain boundary density (Fig. 12(a)), indicating proliferation of subgrain boundaries and dislocations under elevated stress states. Continuous diffraction rings and the presence of high-Miller-index planes in the SAED pattern (Fig. 12(f)) confirm grain rotation and slip during sliding contact. Furthermore, cyclic loading drives progressive reorientation of grains from perpendicular to parallel alignment relative to the surface. Under high shear stresses, grain slip/rotation and severe lattice distortion at GBs culminate in extensive amorphous phase formation (Fig. 12(b and c)). Amorphization is a rare deformation form for metals, due to their malleable lattices and high dislocation tolerance. Zhao [57] reported similar amorphization complementing dislocation glide, twinning, and phase transformation in CrMnFeCoNi high-entropy alloys (HEAs), where high configurational entropy and lattice distortion stabilize shear-induced amorphous phases energetically. Compared to metals, CrN's complex rock-salt structure and strong covalent bonds result in limited strain tolerance and greater susceptibility to amorphization. Each Cr atom is coordinated exclusively with N atoms (1st neighbors) and Cr atoms (2nd neighbors), creating topological constraints. Grain boundaries impede dislocation motion, causing pile-ups that generate extreme lattice distortion and local strain concentrations (Fig. 12(d–g)). This disrupts atomic periodicity more severely than in metallic systems due to directional bonding. Consequently, GBs in CrN become preferential sites for amorphization following severe shear deformation, as periodicity collapse lowers the energy barrier for crystal-to-amorphous transition. Amorphous means the strain limit of crystal lattice is reached and is a indication to cracking.

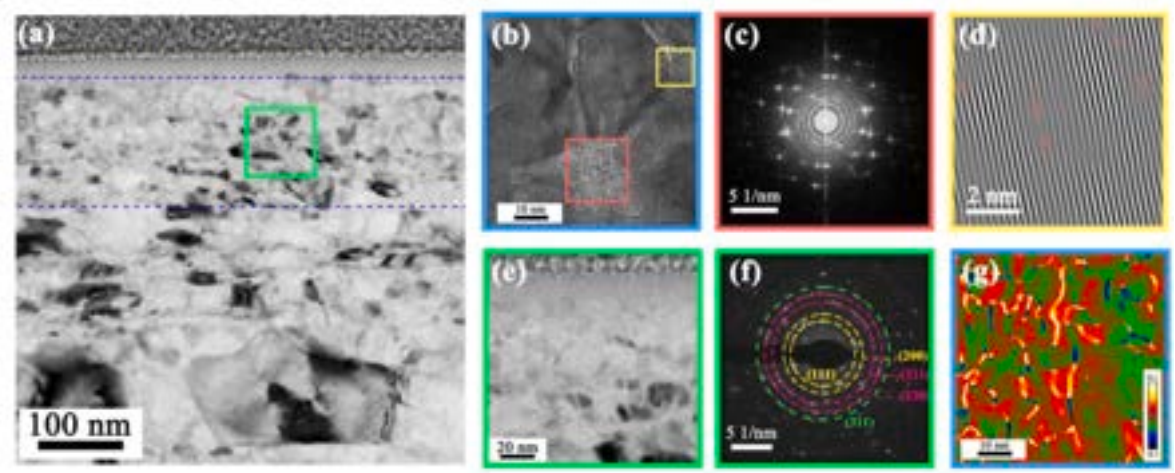

Fig. 12. (a) Equiaxed nanograin layer of CrN film, (b) enlarged view (amorphous region) with (c) SAED, (d) IFFT and (g) GPA of the interface (yellow box in b), (e) enlarged view of nanocrystalline-amorphous layer with (f) SAED. (For interpretation of the references to colour in this figure legend, the reader is referred to the Web version of this article.)

4.3. Comparison between the composite coating and the single-layer CrN film

The cross-sectional TEM image of the wear track of the CrN/NiCrBSi composite coating is similar to that of the single-layer CrN film, as shown in Fig. 13(a), also consisting of an equiaxed nanograin layer, a plastic deformation layer, and an undeformed layer. However, the thickness of the equiaxed nanograin layer in the duplex coating is approximately 230 nm, which is smaller than the 460 nm observed in the CrN film (Figs. 10(a) and 13(d,e)). Furthermore, within the plastic deformation layer, dislocation motion and entanglement lead to the fragmentation of columnar grains into finer equiaxed grains. The average grain size (measured by linear intercept method, ASTM E112-13) in plastic deformation layer of CrN film is about 300.64 nm, while in the CrN/NiCrBSi coating, the average grain size is about 619.47 nm (Fig. 13(b,c)), the grain size in the plastic deformation layer of the CrN/NiCrBSi coating is larger than that of the CrN film. Additionally, distinct cracks are observed within the wear track of the CrN film. These observations collectively suggest that under the same friction conditions, the CrN film undergoes more severe deformation than the CrN/NiCrBSi coating, resulting in a thicker equiaxed nanograin layer, finer grains in the plastic deformation layer, and the occurrence of cracks. This demonstrates that the presence of the HVOF interlayer in the composite coating provides enhanced support, reducing the extent of deformation of the top layer at high-temperatures, delaying crack initiation and failure, and thereby improving the high-temperature wear resistance of the composite coating.

5. Conclusion

This work demonstrates that a load-bearing composite architecture, combining a CrN top layer with HVOF NiCrBSi or Stellite12 interlayers, provides an effective pathway to achieve robust high-temperature wear resistance in nitride ceramic coatings. The composite design not only stabilizes the CrN film during severe thermomechanical loading, but also fundamentally alters its wear response at temperatures up to 600 °C.

The key findings from this work are as follows:

1. The HVOF-supported composite architecture markedly enhances high-temperature hardness, load-bearing capacity, and wear resistance, delivering consistently lower wear rates than monolithic CrN across 200–600 °C.
2. Superior tribological performance in the composite coatings originates from the strong mechanical support of the HVOF interlayer, which suppresses substrate plasticity, reduces subsurface stress concentrations, and delays crack initiation and propagation in the CrN top layer.
3. High-temperature reciprocating sliding activates a hierarchy of deformation mechanisms in CrN, including full and partial dislocation slip, the formation of stacking faults and nanotwins, and localized grain-boundary amorphization. Although these mechanisms improve strain accommodation, they are insufficient to prevent severe damage in monolithic CrN, demonstrating the necessity of external structural support.
4. The introduction of the HVOF interlayer shifts the dominant wear mode from combined oxidative, abrasive, and fatigue wear in monolithic CrN to predominantly mild oxidative wear in the composite coating, revealing a stabilized surface and reduced subsurface degradation.
5. The composite coating concept provides both mechanistic insights and a practical design strategy for achieving high-temperature wear-resistant ceramic coatings, highlighting the value of integrating microstructure engineering with architecture-driven load-bearing design.

CRediT authorship contribution statement

Lei Shao: Writing – review & editing, Supervision, Data curation, Conceptualization. **Ru Liu:** Writing – original draft, Investigation. **Wensheng Li:** Writing – review & editing, Project administration, Funding acquisition. **Yanru Sun:** Writing – original draft, Formal analysis, Data curation, Conceptualization. **Xuedan Song:** Data curation. **Xiaojie Song:** Formal analysis. **Canming Wang:** Methodology. **Qiang Song:** Methodology. **Lunlin Shang:** Resources, Methodology. **Sheng Guo:** Methodology.

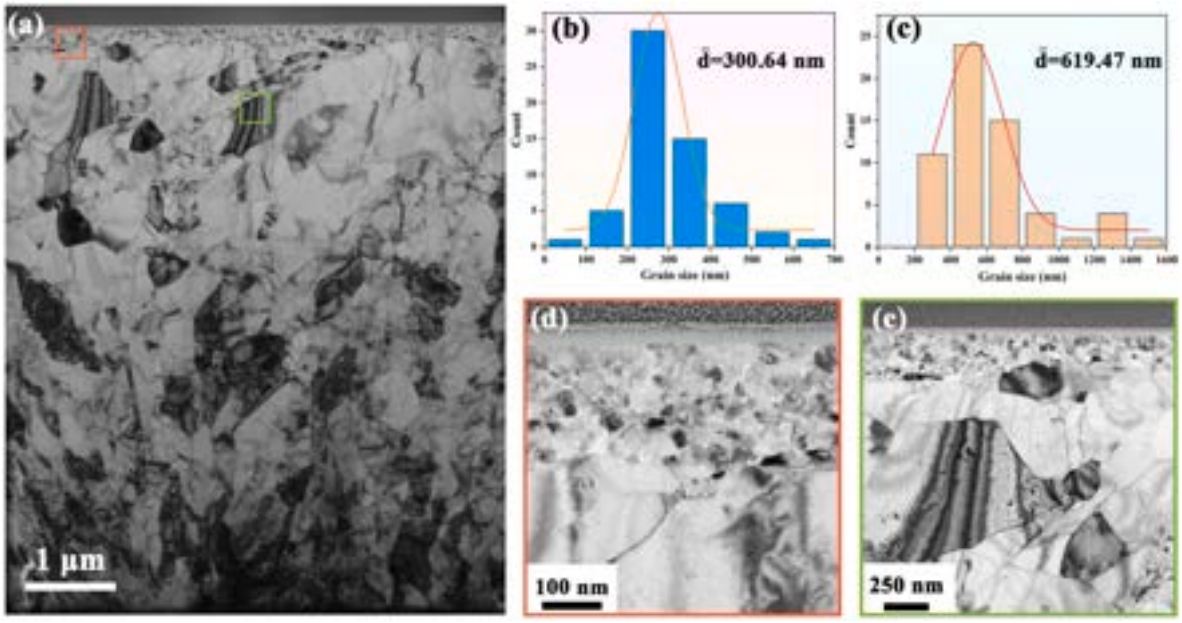

Fig. 13. Cross-sectional TEM in wear track of CrN/NiCrBSi coating (a), grain size in equiaxed nanograin layer of CrN (b) and CrN/NiCrBSi (c), partial enlarged image (d,e).

Declaration of competing interest

The authors declare that they have no known competing financial interests or personal relationships that could have appeared to influence the work reported in this paper.

Acknowledgments

This study was supported by National Natural Science Foundation of China (52305204, 52471081), Major Basic Research Project in Shandong Province (ZR2022ZD13), and Taishan Scholarship (tstp20221127).

Data availability

Data will be made available on request.

References

[1] Sathish M, Radhika N, Saleh B. A critical review on functionally graded coatings: methods, properties, and challenges. Compos Pt B-Eng 2021;225:109278.
[2] Xu ZG, Li DG, Wang PP, Jiang LT, Chen GQ, Wu GH. Effect of TM (TM=Fe, Mn, Cr) alloying on the high temperature properties and strengthening mechanism of C_f/Al composites. Compos Pt B-Eng 2021;211:108622.
[3] Chen Z, Zheng YH, Löfler L, Bartosik M, Sheng HP, Gammer C, Holec D, Zhang ZL. Real-time atomic-resolution observation of coherent twin boundary migration in CrN. Acta Mater 2021;208:116732.
[4] Du JW, Chen L, Chen J, Hu C. Influence of oxygen addition on the structure, mechanical and thermal properties of CrN coating. Surf Coat Technol 2021;411:126992.
[5] Zhao XB, Yan DR, Li S, Lu CG. The effect of heat treatment on the electrochemical corrosion behavior of reactive plasma-sprayed TiN coatings. Appl Surf Sci 2011;257(23):10078–83.
[6] Chen YM, Go T, Pang XL, Qiao LJ. Formation of high-density stacking faults in ceramic films induced by Ti transition layer. Scr Mater 2022;211:114496.
[7] Zhang M, Hu XG, Yang XX, Xu FF, Kim KH, Shao ZG. Influence of substrate bias on microstructure and morphology of ZrN thin films deposited by arc ion plating. Trans Nonferrous Met Soc China 2012;22:s115–9.
[8] Peters AB, Wang CH, Zhang DJ, Hernandez A, Nagle DC, Mueller T, Spicer JB. Reactive laser synthesis of ultra-high-temperature ceramics HfC, ZrC, TiC, HfN, ZrN, and TiN for additive manufacturing. Ceram Int 2023;49(7):11204–29.
[9] Chang YY, Weng SY, Chen CH, Fu FX. High temperature oxidation and cutting performance of AlCrN, TiVN and multilayered AlCrN/TiVN hard coatings. Surf Coat Technol 2017;332:494–503.
[10] Chen WL, Hu T, Hong Y, Zhang DD, Meng XN. Comparison of microstructures, mechanical and tribological properties of arc-deposited AlCrN, AlCrBN and CrBN coatings on Ti-6Al-4V alloy. Surf Coat Technol 2020;404:126429.
[11] Drnovšek A, Vo HT, Figueiredo MR, Kolozsvári S, Hosemann P, Franz R. High temperature fracture toughness of single-layer CrAlN and CrAlSiN hard coatings. Surf Coat Technol 2021;409:126909.
[12] Xu YX, Chen L, Liu ZQ, Pei F, Du Y. Improving thermal stability of TiSiN nanocomposite coatings by multilayered epitaxial growth. Surf Coat Technol 2017;321:180–5.
[13] Hu C, Chen L, Lou YM, Zhao NN, Yue JL. Influence of Si content on the microstructure, Thermal Stability and Oxidation Resistance of TiAlSiN/CrAlN Multilayers. J Alloys Compd 2021;855:157441.
[14] Chen Z., Wang Y., Chen X., Huang C., Xu S., Xu Q., Zhao S., Kujawski W., Zhang P., Ultrathin nanocomposite membrane with robust anti-wettability for stable membrane distillation. *Interdiscip. Mater.* 2025; 4 (4): 610-619.
[15] Hörling A, Hultman L, Odén M, Sjölén J, Karlsson L. Mechanical properties and machining performance of $Ti_{1-x}Al_xN$coated cutting tools. Surf Coat Technol 2005;191(2–3):384–92.
[16] Liu AH, Duan JX, Cui HB, Chen YY, Zhao J. Friction and wear properties of TiN, TiAlN, AlTiN and CrAlN PVD nitride coatings. Int J Refract Met Hard Mater 2012;31:82–8.
[17] Grossmann B, Schalk N, Czettl C, Pohler M, Mitterer C. Phase composition and thermal stability of arc evaporated $Ti_{(1-x)}Al_xN$ hard coatings with $0.4 \leq x \leq 0.67$. Surf Coat Technol 2017;309:687–93.
[18] Todt J, Zalesak J, Daniel R, Pitonak R, Köpf A, Weißenbacher R, Sartory B, Mitterer C, Keckes J. Al-rich cubic A1(0.8)Ti(0.2)N coating with self-organized nano-lamellar microstructure: thermal and mechanical properties. Surf Coat Technol 2016;291:89–93.
[19] Holec D, Rovere F, Mayrhofer PH, Barna PB. Pressure-dependent stability of cubic and wurtzite phases within the TiN-AlN and CrN-AlN systems. Scr Mater 2010;62(6):349–52.
[20] Euchner H, Mayrhofer PH. Vacancy-dependent stability of cubic and wurtzite $Ti_{1-x}Al_xN$. Surf Coat Technol 2015;275:214–8.
[21] Zhao L, Munroe P, Jiang ZT, Zhao XL, Xu J, Zhou ZF, Jiang JQ, Feng F, Xie ZH. Designing superhard, self-toughening CrAlN coatings through grain boundary engineering. Acta Mater 2012;60(16):5735–44.
[22] Soleimani M, Fattah-alhosseini A, Elmkhah H, Babaei K, Imantalab O. A comparison of tribological and corrosion behavior of PVD-deposited CrN/CrAlN and CrCN/CrAlCN nanostructured coatings. Ceram Int 2023;49(3):5029–41.
[23] Liu JK, Cui ZX, Ma DY, Lu JQ, Cui YG, Li C, Liu WB, Hao Z, Hu PF, Yao MY, Huang P, Bai GH, Yun D. Investigation of oxidation behaviors of coated zircaloy as accident-tolerant fuel with CrAlN and CrAlSiN coatings in high-temperature steam. Corros Sci 2020;175:108896.
[24] Hu C, Chen L, Lou YM, Zhao NN, Yue JL. Influence of Si content on the microstructure, thermal stability and oxidation resistance of TiAlSiN/CrAlN multilayers. J Alloys Compd 2021;855:157441.
[25] Wang QM, Kim KH. Microstructural control of Cr-Si-N films by a hybrid arc ion plating and magnetron sputtering process. Acta Mater 2009;57(17):4974–87.
[26] Carvalho NJM, De-Hosson JTM. Deformation mechanisms in TiN/(Ti,Al)N multilayers under depth-sensing indentation. Acta Mater 2006;54(7):1857–62.
[27] Zhou C, Dong C, Wang W, Tian Y, Shen C, Yan K, Mai L, Xu X. An ultrathin and crack-free metal-organic framework film for effective polysulfide inhibition in lithium-sulfur batteries. Interdiscip. Mater 2024;3(2):306–15.
[28] Li CL, Wang LG, Shang LL, Cao XQ, Zhang GA, Yu Y, Li WS, Zhang SZ, Hu HT. Mechanical and high-temperature tribological properties of CrAlN/TiSiN multilayer coating deposited by PVD. Ceram Int 2021;47(20):29285–94.
[29] Sun YR, Shao L, Li WS, Shang LL, Wang CM, Song Q, Zhang CZ. Effect of Stellite12 and NiCrBSi HVOF coatings on the tribological behavior of CrN PVD film. Tribol Int 2024;198:109880.
[30] Yu HY, Liang WP, Miao Q, Yin MJ, Ma YY, Zuo SW. Effect of shot peening pretreatment on the high-temperature tribological behaviours of a TaN coating prepared via double-cathode glow plasma alloying. Surf Coat Technol 2021;427:127825.
[31] Daniel R, Martinschitz KJ, Keckes J, Mitterer C. The origin of stresses in magnetron-sputtered thin films with zone T structures. Acta Mater 2010;58(7):2621–33.
[32] Vasco E, Polop C. Intrinsic compressive stress in polycrystalline films is localized at edges of the grain boundaries. Phys Rev Lett 2017;119(25):256102.
[33] Scharf TW, Prasad SV. Solid lubricants: a review. J Mater Sci 2013;48(2):511–31.
[34] Zauner L, Hahn R, Aschauer E, Wojcik T, Davydok A, Hunold O, Polcik P, Riedl H. Assessing the fracture and fatigue resistance of nanostructured thin films. Acta Mater 2022;239:118260.
[35] Verma N, Cadambi S, Jayaram V, Biswas SK. Micromechanisms of damage nucleation during contact deformation of columnar multilayer nitride coatings. Acta Mater 2012;60(6–7):3063–73.
[36] Xie ZH, Hoffman M, Munroe P, Bendavid A, Martin PJ. Deformation mechanisms of TiN multilayer coatings alternated by ductile or stiff interlayers. Acta Mater 2008;56(4):852–61.
[37] Pantleon W. Resolving the geometrically necessary dislocation content by conventional electron backscattering diffraction. Scr Mater 2008;58(11):994–7.
[38] Zhu XH, Yang XS, Huang WJ, Liu YJ, Qiu WY, Wang X, Li MD. Influence of precipitation on geometrically necessary dislocations distribution and fracture behavior in an Al-Cu-Li alloy. J Alloys Compd 2025;1013:178561.
[39] Toth LS, Gu CF, Beausir B, Fundenberger JJ, Hoffman M. Geometrically necessary dislocations favor the taylor uniform deformation mode in ultra-fine-grained polycrystals. Acta Mater 2016;117:35–42.
[40] Zhong HR, Shi QW, Dan CY, You XJ, Zong SW, Zhong SY, Zhang YD, Wang HW, Chen Z. Resolving localized geometrically necessary dislocation densities in Al-Mg polycrystal via in situ EBSD. Acta Mater 2024;279:120290.
[41] Velasco L, Hodge AM. The mobility of growth twins synthesized by sputtering: tailoring the twin thickness. Acta Mater 2016;109:142–50.
[42] Zhang Y, Liu ZR, Yuan DW, Shao Q, Chen JH, Wu CL, Zhang ZL. Elastic properties and stacking fault energies of borides, carbides and nitrides from first-principles calculations. Acta Metall Sin (Engl Lett) 2019;32(9):1099–110.
[43] Zhang X, Misra A, Wang H, Shen TD, Nastasi M, Mitchell TE, Hirth JP, Hoagland RG, Embury JD. Enhanced hardening in Cu/330 strainless steel multilayers by nanoscale twinning. Acta Mater 2004;52(4):995–1002.
[44] Bufford D, Wang H, Zhang X. High strength, exitaxial nanotwinned Ag films. Acta Mater 2011;59(1):93–101.
[45] Britun VF, Kurdyumov AV. Mechanisms of martensitic transformations in boron nitride and conditions of their development. High Press Res 2000;17(2):101–11.
[46] Tian YJ, Xu B, Yu DL, Ma YM, Wang YB, Jiang YB, Hu WT, Tang CC, Gao YF, Luo K, Zhao ZS, Wang LM, Wen B, He JL, Liu ZY. Ultrahard nanotwinned cubic boron nitride. Nature 2013;493(7432):385–8.
[47] Huang Q, Yu QL, Xu B, Hu WT, Ma YM, Wang YB, Zhao ZS, Wen B, He JL, Liu ZY, Tian YJ. Nanotwinned diamond with unprecedented hardness and stability. Nature 2014;510(7504):250–3.
[48] Chen Z, Shao QQ, Bartosik M, Mayrhofer PH, Chen H, Zhang ZL. Growth-twins in CrN/AlN multilayers induced by hetero-phase interfaces. Acta Mater 2020;185:157–70.
[49] Li N, Yadav SK, Liu XY, Wang J, Hoagland RG, Mara N, Misra A. Quantification of dislocation nucleation stress in TiN through high-resolution in situ indentation experiments and first principles calculations. Sci Rep 2015;5(1):15813.
[50] Su RZ, Neffati D, Zhang YF, Cho J, Li J, Wang HY, Kulkarni Y, Zhang XH. The influence of stacking faults on mechanical behavior of advanced materials. Mater Sci Eng, A 2021;803:140696.
[51] Velasco L, Hodge AM. Growth twins in high stacking fault energy metals: microstructure, texture and twinning. Mater Sci Eng, A 2017;687:93–8.
[52] Chen YM, Yan XY, Guo T, Ma Y, Mi ZS, Pang XL, Qiao LJ. Cross-interface growth mechanism of nanotwins in extremely high stacking-fault energy ceramic layer. Acta Mater 2023;257:119189.

[53] Zhang YF, Su R, Niu TJ, Richter NA, Xue S, Li Q, Ding J, Yang B, Wang H, Zhang X. Thermal stability and deformability of annealed nanotwinned Al/Ti multilayers. Scr Mater 2020;186:219–24.
[54] Zhou SH, Qiu ZG, Zeng DC. Deformation mechanisms and crack routes of CrAlN coatings. Mater Charact 2020;167:110491.
[55] Zhang X, Misra A, Wang H, Nastasi M, Embury JD, Mitchell TE, Hoagland RG, Hirth JP. Nanoscale-twinning-induced strengthening inaustenitic stainless steel thin films. Appl Phys Lett 2004;84:1096–8.
[56] Yue YH, Gao YF, Hu WT, Xu B, Wang J, Zhang XJ, Zhang Q, Wang YB, Ge BH, Yang ZY, Li ZH, Ying P, Liu XX, Yu DL, Wei B, Wang ZC, Zhou XF, Guo L, Tian YJ. Hierarchically structured diamond composite with exceptional toughness. Nature 2020;582:370–4.
[57] Zhao ST, Li ZZ, Zhu CY, Yang W, Zhang ZR, Armstrong DEJ, Grant PS, Ritchie RO, Meyers MA. Amorphization in extreme deformation of the CrMnFeCoNi high-entropy alloy. Sci Adv 2021;7:3108–37.